2021

A semi-empirical model for thermal resistance and dryout during boiling in thin porous evaporators fed by capillary action

S. Sudhakar

J.A. Weibel

S.V. Garimella

Sudhakar, S.; Weibel, J.A.; and Garimella, S.V., "A semi-empirical model for thermal resistance and dryout during boiling in thin porous evaporators fed by capillary action" (2021). *CTRC Research Publications.* Paper 388.
http://dx.doi.org/10.1016/j.ijheatmasstransfer.2021.121887

A Semi-Empirical Model for Thermal Resistance and Dryout during Boiling in Thin Porous Evaporators fed by Capillary Action

Srivathsan Sudhakar, Justin A. Weibel[1], Suresh V. Garimella[2]

School of Mechanical Engineering

Purdue University, 585 Purdue Mall, West Lafayette, IN 47907 USA

Abstract

Two-phase passive heat transport devices such as vapor chambers, loop heat pipes, and capillary pumped loops utilize porous evaporators for phase change and to drive fluid transport. Nucleate boiling can occur within such capillary-fed porous evaporators, especially under high-heat-flux operation, as has been visually observed in various experimental studies in the literature. However, prior modeling efforts have typically only considered single-phase flow of liquid through a completely saturated porous medium for characterizing the dryout limit and thermal performance. The present work offers a new semi-empirical model for prediction of thermal resistance and dryout during boiling in capillary-fed evaporators. Thermal conduction across the solid and volumetric evaporation within the pores are solved to obtain the temperature distribution in the porous structure. Capillary-driven lateral liquid flow from the outer periphery of the evaporator to its center, with vapor flow across the thickness, is considered to obtain the local liquid and vapor pressures. The capillary pressure and the relative permeabilities (fraction of single-phase permeabilities) for two-phase flow in the porous medium are modeled as a function of the local liquid saturation. The heat flux at which the liquid saturation at the center of the evaporator becomes zero is defined as the dryout limit of the evaporator. Experiments are conducted on sintered copper particle evaporators of different particle sizes and heater areas to collect data for model calibration. To demonstrate the wider applicability of the model for other types of porous evaporators, the model is further calibrated against a variety of dryout limit and thermal resistance data collected from the literature. The model is shown to predict the experimentally observed trends in the dryout limit with mean particle/pore size, heater size, and evaporator thicknesses.

Keywords

Dryout, thermal resistance, capillary-fed boiling, capillary pressure, relative permeability, evaporator, liquid saturation

---

[1] Corresponding author, E-mail address: jaweibel@purdue.edu.
[2] Currently President, University of Vermont

Nomenclature

A	area (m^2)
C_E	Ergun coefficient (–)
d	wire/pillar diameter (m)
D	mean particle diameter (m)
h	heat transfer coefficient (W/m^2K)
$\tilde{h}_{evap}$	volumetric evaporation heat transfer coefficient (W/m^3K)
h_{fg}	heat of vaporization (J/kgK)
k	thermal conductivity (W/mK)
K	permeability (m^2)
$\dot{m}$	mass flow rate (kg/s)
n	saturation exponent in $K_{rl} = s^n$ (–)
N	number of pores in a control volume (–)
P	pressure (Pa)
q	heat flux (W/m^2)
$\tilde{q}$	volumetric heat flux (W/m^3)
Q	heat transfer rate (W)
r	radius*;* radial coordinate (m)
R	specific gas constant (J/kgK)
R_{th}	thermal resistance (K/W)
s	liquid saturation (–)
t	thickness/height (m)
T	temperature (K)
u	velocity (m/s)
v_{fg}	specific volume change (m^3/kg)
z	z coordinate (m)

Greek symbols

μ	dynamic viscosity (kg/ms)
ν	kinematic viscosity (m^2/s)
ρ	density (kg/m^3)
σ	surface tension (N/m); accommodation coefficient (–)
φ	porosity (–)

δ effective film thickness (m)

θ evaporator superheat (K)

Subscripts

avg average

boil capillary-fed boiling

c capillary

cond conduction

Cu copper

CV control volume

dry dryout

e evaporator

eff effective

evap evaporation

l liquid

lv liquid–vapor interface

max maximum

meas measured

pore single pore in a control volume

rl relative liquid

rv relative vapor

s solid

sat saturation

sub substrate

w wall

wick refers to evaporator wick

v vapor

1 Introduction

The drive for increased power densities and miniaturization of electronic systems in power conversion, communications, and high-performance computing applications has led to high heat fluxes at the semiconductor die-level, requiring advanced thermal management materials and strategies [1]. To enable reliable operation of electronics, effective heat rejection to the surroundings is critical. As a result, research in thermal management has focused on developing techniques to dissipate high fluxes from compact spaces

across a low thermal resistance. Two-phase heat transport devices such as conventional heat pipes and vapor chambers [2], capillary pumped loops (CPLs) and loop heat pipes (LHPs) [3,4] are attractive for heat transport and spreading in thermal management applications, due to their reliability and passive operation.

Porous evaporators for phase change transport and capillary feeding of liquid are commonly deployed in these devices. Subject to a heat load at the evaporator, the working fluid contained in the porous evaporator vaporizes, thereby transporting the heat to the condenser where it is dissipated typically over a greater area. The vapor is thus condensed, and liquid is pumped back to the evaporator by capillary action due to menisci sustained in the pores. The maximum heat transport capability of the porous medium is governed by the maximum capillary pressure ($P_{c,max}$) available at the evaporator, which must overcome the liquid flow pressure drop (ΔP_l). Under low-heat flux operation, the single-phase liquid pressure drop can be readily predicted for flow through porous media. However, when high heat fluxes (exceeding ~100 W/cm^2, for example) are imposed, nucleate boiling can occur in the porous medium; this 'capillary-fed boiling' process has been observed in a number of studies in the literature [5,6,7,8,9]. These experiments have characterized the dryout heat flux and thermal resistance during capillary-fed boiling within different types of porous evaporators (including sintered particles [6], sintered screen mesh [7], and micro-pillars [8,9]).

In contrast to these experimental efforts, prior models have not arrived at a first-principles-based, mechanistic prediction of the dryout heat flux and thermal resistance of an evaporator with known effective properties. Any analytical prediction of the thermal performance is complicated by the stochastic nature of boiling in porous media. Full-scale, two-phase mixture models have been proposed for transport in porous media [10], but such formulations can become complicated, especially if accounting for phase change. As an alternative to reduce the complexity in modeling phase change within highly tortuous porous evaporators, pore-network simulations are utilized (e.g., see Refs. [11,12] for loop heat pipe performance prediction). We motivate the need for a new thermo-fluidic model for capillary-fed boiling, based on the review below of analytical and empirical models in the literature involving the simultaneous flow of two phases (liquid and vapor) in porous media, albeit for different applications.

Analytical and empirical models are available for the prediction of critical heat flux (CHF) in pool boiling from porous coated surfaces that are submerged in the working fluid. Liter and Kaviany [13]modeled CHF in saturated pool boiling considering the liquid/vapor counter-current flow hydrodynamics within the porous structure. The length scale of locations for vapor to escape from the surface into the liquid pool was predicted to affect the CHF. The authors therefore concluded that modulating the geometry of the porous coating to alter the length scale of vapor-escape locations can significantly improve CHF compared to pool boiling over plain surfaces. Webb [14] and Rao and Balakrishnan [15] also developed simplified analytical models for pool boiling from porous coated surfaces.

Other works (e.g., Chang and You [16]) have experimentally studied the effect of particle size in pool boiling over microporous diamond surfaces and developed an empirical correlation for the CHF as a function of mean particle diameter by fitting to data.

Critical heat flux (CHF) models for pool boiling from submerged porous-coated surfaces are not directly applicable to the prediction of dryout during capillary-fed boiling in porous evaporators. In pool boiling, models posit that CHF is governed by stability of the liquid-vapor counterflow (e.g., Zuber's limit [17]), in addition to viscous drag resistance imposed by the solid matrix on the liquid-vapor counterflow [13]. In contrast, the liquid flow in capillary-fed evaporators occurs laterally into the heated region, with a limit that is governed by the liquid flow pressure drop from the edge of the evaporator (from where liquid is fed) to the center. Consequently, the heater size, and thus the capillary-feeding length, more dramatically affect the dryout heat flux during capillary-fed boiling [18] than in pool boiling [13].

The maximum heat flux sustained by a thick bed of liquid-saturated porous particles (heated on one end) was modeled by Udell [19] and Bau and Torrance [20]. Considering one-dimensional, steady, two-phase counter-current flow in the bed, these models assumed three separate zones for heat transfer: namely, a vapor zone closest to the heated end, an intermediate two-phase zone, and then a saturated liquid zone, as shown schematically in Figure 1 (a). Temperature gradients were neglected within the two-phase zone (isothermal zone) and the flow of liquid and vapor phases were governed by Darcy's law. While heated from below, downward liquid flow through the bed is driven by capillary action and gravity, while upward vapor flow is driven by buoyancy forces. The local liquid saturation (the fraction of porous volume filled with liquid) is minimum at the bottom of the two-phase zone and increases monotonically along the thickness of the bed (see Figure 1 (a)). The saturation profiles exhibit step changes on either end of the two-phase zone (minimum value is higher than zero due to an irreducible saturation, as described by Udell [19]). Counter-current flow models [19, 20] are used extensively in applications involving two-phase flows in heated particulate beds to find the length of the two-phase zone and the critical (maximum) heat flux sustained by the bed.

Tung and Dhir [21] developed analytical pressure drop models for two-phase flow (both co-current and counter-current) in porous media. All of these models [19-21] utilize relative permeability (i.e., the permeability of each phase within the porous media in the presence of the other phase), typically modeled as a function of the local liquid saturation. The widely used correlations for relative permeability (most commonly taking the form $K_l = s^n$) are tabulated by Scheidegger [22] and Kaviany [23]. Predictions for two-phase flow in porous media rely heavily on the availability and accuracy of expressions for relative permeability for the specific porous medium of interest. Therefore, two-phase flow models developed for thick macro-scale porous beds (with relative permeability correlations found from experimental

measurements on such beds) cannot be directly applied to capillary-fed boiling in micro-scale porous evaporators.

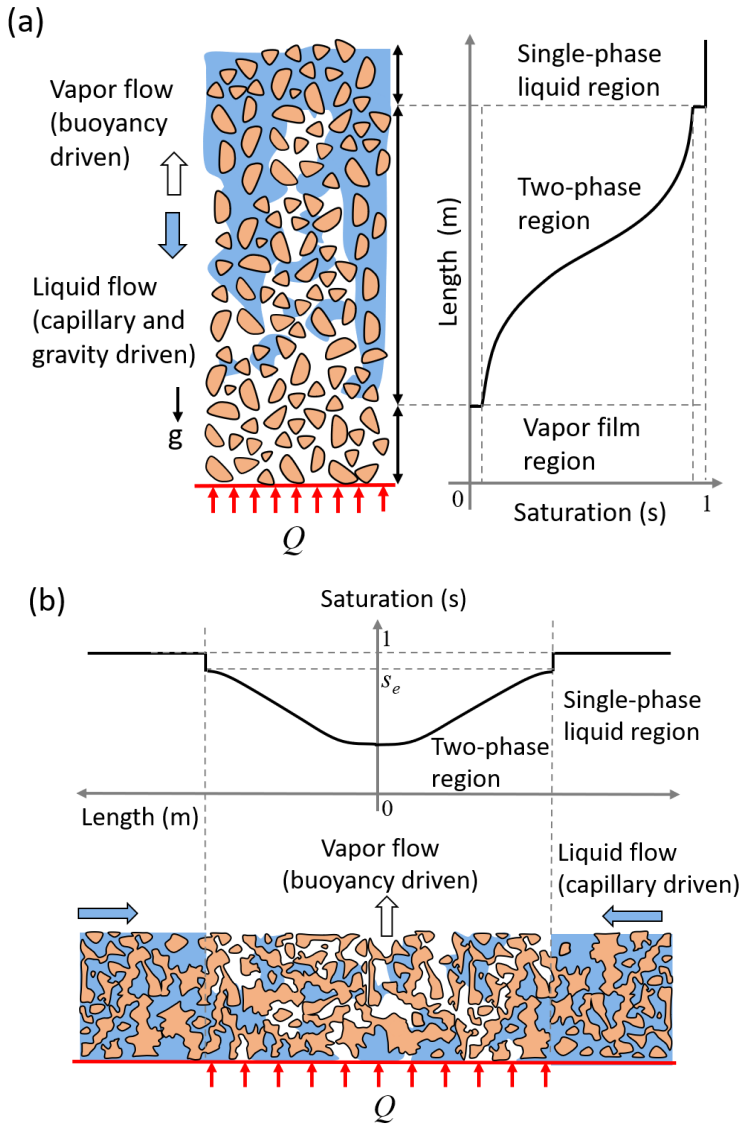

Figure 1. (a) The two-phase flow configuration (liquid-vapor counterflow) and the associated saturation profiles in a packed bed of porous particles heated from below, as described by Udell [19] and Bau and Torrance [20]. (b) The flow configuration of interest in this work and saturation profiles during boiling in capillary-fed porous evaporators. (Note to editor: 1 column wide)

The current work presents a new semi-empirical approach to calculating the dryout limit and thermal resistance during capillary-fed boiling, specifically in thin porous evaporators commonly used in two-phase heat transport devices. Figure 1 (b) schematically shows the flow configuration of interest in such porous

evaporators. Lateral liquid flow is driven by capillary action from a single-phase region to the center of the two-phase region (the heated zone); vapor flow occurs through the thickness of the porous media. The liquid saturation profile decreases from its maximum value at the edge of the two-phase region to a minimum value at the center. Thermal conduction in the solid structure in the thickness direction, and volumetric pore-scale evaporation within the porous structure, are modeled to obtain the temperature distribution and the thermal resistance. The governing Darcy-Ergun equation (in radial coordinates), corrected for the relative permeability for two-phase flow, is used to solve the hydrodynamics within the evaporator domain. The dryout limit of the evaporator is defined as the input heat flux at which the liquid saturation at the center of the domain reduces to zero. We perform experiments using sintered copper particle wicks of different particle sizes and heater areas, and also survey the literature for additional experiments, to collect data for broad calibration of the model across a variety of porous evaporators.

2 Model Formulation

A cylindrical domain of radius r_e and thickness t as shown in Figure 2 (a) is considered as the porous evaporator. A heat input Q_w is supplied at the base wall (at $z = 0$) and the evaporator transports saturated liquid in by wicking action from the periphery at a constant rate ($\dot{m}_l = Q_w/h_{fg}$). Phase change occurs within the region and the vapor thus formed is assumed to flow out through the thickness (in the z direction). The vapor pressure is highest at the base of the evaporator ($z = 0$) and decreases to the saturation vapor pressure at the top (i.e., $P_v = P_{sat}$ at $z = t$, where P_{sat} is the saturation pressure). The following assumptions are made regarding the flow and heat transfer in this modeling framework:

1. At a given heat input Q_w, boiling is assumed to be occurring uniformly over the entire evaporator area.
2. The liquid flows one-dimensionally in the radial direction, from the outer periphery where it is fed ($r = r_e$) to the center of the domain ($r = 0$), evaporating completely. Thus, the liquid pressure is a function of the radial coordinate r only.
3. The vapor formed flows one-dimensionally in the axial direction from the wall ($z = 0$) through the porous evaporator thickness (to $z = t$).
4. Heat transfer occurs by one-dimensional conduction (in the z direction) from the heated wall through the solid porous matrix, by evaporation into the open pores within the porous medium, and ultimately to the saturated vapor above. Radial conduction in the porous evaporator structure is neglected.
5. The temperature of the saturated vapor within the pore spaces along the thickness of the evaporator is uniform and equal to the saturation temperature T_{sat} (*i.e.,* the saturation

temperature change, due to the viscous vapor flow pressure drop through the thickness direction is very small and therefore neglected).

In the following subsections, the heat transfer relations are first presented to predict the temperature distribution and the thermal resistance, and the flow relations for the pressure drop and dryout limit prediction follow.

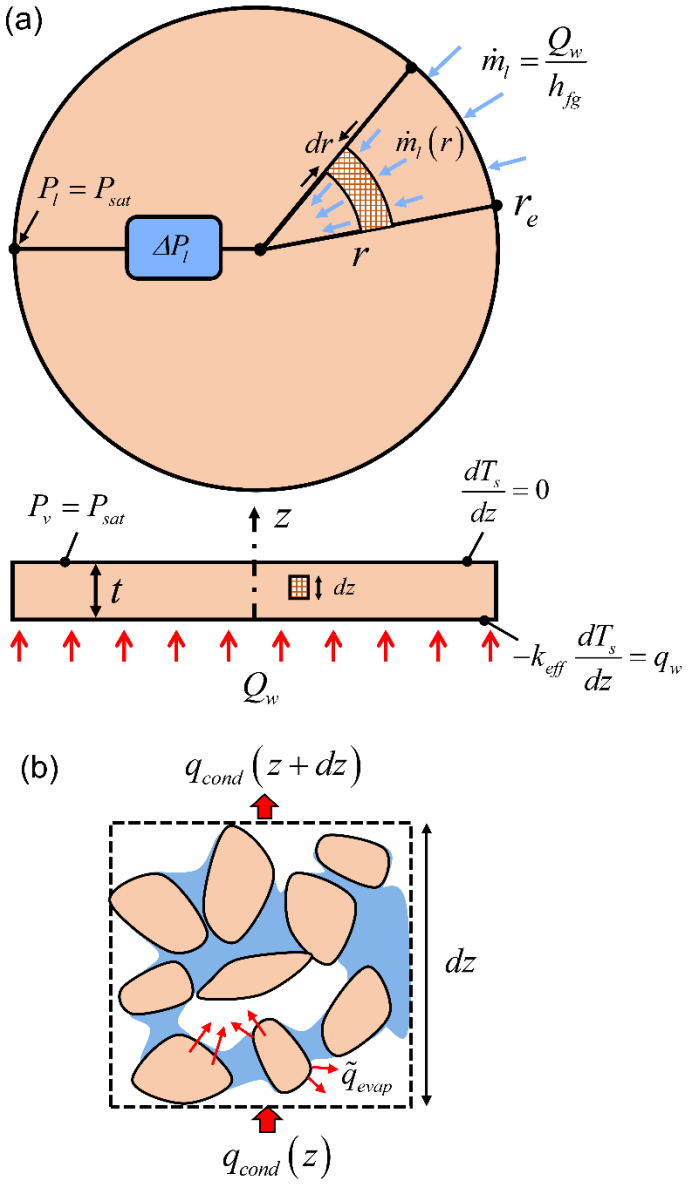

Figure 2. (a) Top-down view and cross-sectional side view schematic diagrams showing the geometry and boundary conditions for the cylindrical porous evaporator solution domain. The heat input is applied over a radius r_e over which boiling occurs. (b) A control volume considered in the thickness direction for the heat transfer model. (note to editor: 1 column wide).

2.1 Heat transfer relations and prediction of thermal resistance

Heat transfer from the base surface occurs by conduction through the solid matrix, followed by volumetric evaporation occurring in the open pores within the domain. Kovalev *et al.* [24] followed the same approach to model the temperature distribution within porous coated surfaces in pool boiling. A control volume as shown in the side view schematic diagram of Figure 2 (a) is chosen to develop the governing heat transfer equations. It is assumed that the control volume consists of a representative elementary volume of particles and pores (as shown in Figure 2 (b)), in which volume-averaged quantities such as solid and liquid temperatures can be defined. The pore spaces between the particles are filled with liquid and vapor phases. An energy balance equation in the control volume can be written based on the conduction and evaporation fluxes:

$$\begin{aligned} &\frac{d\left(q_{cond}\right)}{dz}+\tilde{q}_{evap}=0 \\ &\text{where} \\ &q_{cond}=-k_{eff}\frac{dT_s}{dz} \\ &\tilde{q}_{evap}=\tilde{h}_{evap}\left(T_s-T_{sat}\right) \end{aligned} \tag{1}$$

In the above equation, q_{cond} is the conduction flux in the *z*-direction and $\tilde{q}_{evap}$ is the volumetric evaporation flux within the entire control volume. To estimate the volumetric heat transfer coefficient $\tilde{h}_{evap}$, a pore-scale evaporation model is developed, as described in Appendix A. The control volume is modeled as a collection of *N* pores; each pore is assumed to be cylindrical in shape with a nominal effective pore radius r_{eff}. The solid matrix in the pore is covered with an annular liquid film of thickness δ, and the vapor in the pore space occupies the cylindrical region of radius $r_{eff} - \delta$ (refer Figure A.1 in Appendix A).

The analysis in Appendix A provides an expression for the volumetric heat transfer coefficient:

$$\tilde{h}_{evap}=\frac{2\left(r_{eff}-\delta\right)h_{lv}\varphi}{{r_{eff}}^2\left(1+\frac{h_{lv}}{k_l}\left(r_{eff}-\delta\right)\ln\left(\frac{r_{eff}}{r_{eff}-\delta}\right)\right)} \tag{2}$$

Introducing the solid matrix superheat $\theta = T_s - T_{sat}$, the governing energy equation in (1) becomes

$$\frac{d^2\theta\left(z\right)}{dz}=\frac{\tilde{h}_{evap}}{k_{eff}}\theta\left(z\right) \tag{3}$$

The governing energy equation is solved with the boundary conditions,

$$-k_{eff}\left.\frac{d\theta}{dz}\right|_{z=0} = q_w \qquad (4)$$

$$\left.\frac{d\theta}{dz}\right|_{z=t} = 0$$

At the wall surface boundary ($z = 0$), the conduction flux is equal to the wall heat flux q_w because there is no volumetric evaporation at the surface of the wall. An adiabatic condition is assumed at the top surface of the wick ($z = t$), i.e., the conduction flux is zero at the surface (all the supplied heat input is removed through flow of the vapor out of the wick at $z = t$).

Using these boundary conditions, the solution for the temperature profile in the thickness direction can be obtained as

$$\theta(z) = \frac{q_w}{M_e k_{eff}\left(e^{2M_e t} - 1\right)}\left(e^{M_e z} + e^{M_e(2t-z)}\right) \qquad (5)$$

where $M_e = \sqrt{\tilde{h}_{evap}/k_{eff}}$. The capillary-fed boiling thermal resistance of the wick is obtained as

$$R_{th} = \frac{\theta|_{z=0}}{q_w} = \frac{1}{M_e k_{eff}}\frac{\left(e^{2M_e t} + 1\right)}{\left(e^{2M_e t} - 1\right)} = \frac{1}{M_e k_{eff}\tanh\left(M_e t\right)} \qquad (6)$$

In the expression for h_{evap} in equation (2), the effective film thickness δ is the only unknown for a given wick geometry and working fluid combination. The parameter is found by calibrating the predicted thermal resistance to experimental data (for sintered particle wick structures in section 5.2 and with other porous evaporators from the literature in section 5.3). Note that the model formulation inherently assumes a constant value of effective film thickness throughout the evaporator domain to facilitate an analytical solution to the heat transfer equation (eqn. (1)). This choice of model formulation also allows for straightforward calibration of the effective film thickness parameter to experimental measurements.

2.2 Hydrodynamic relations and prediction of dryout

At steady state, the uniform heat input at the bottom of the evaporator Q_w is assumed to be completely utilized to change the phase of the saturated liquid that enters the domain. Accounting for the evaporated mass, the mass flow rate of liquid varies in the radial direction as,

$$\dot{m}_l(r) = \frac{Q_w}{h_{fg}}\frac{r^2}{r_e^2} \qquad (7)$$

The liquid velocity in the radial direction is given by $u_l = \dot{m}_l/(2\pi r t)$. The Ergun equation for flow through porous media is used to obtain the liquid pressure drop in the radial direction,

$$\frac{dP_l(r)}{dr} = \frac{\mu_l}{KK_{rl}} u_l + \frac{\rho_l C_E}{K^{1/2} K_{rl}} u_l^2 \tag{8}$$

where K is the intrinsic single-phase permeability and $C_E = 1.8\,(1-\varphi)\sqrt{K/(D\,\varphi^2)}$ is the Ergun coefficient. To account for the reduction in feeding area due to the presence of vapor in the pores, the single-phase permeability is reduced by a factor K_{rl} (the relative permeability of the liquid phase).

The vapor phase pressure gradient in the thickness direction of the wick is,

$$\frac{dP_v}{dz} = \frac{\mu_v}{KK_{rv}} u_v + \frac{\rho_v C_E}{K^{1/2} K_{rv}} u_v^2 \tag{9}$$

where K_{rv} represents the relative permeability of the vapor phase due to the presence of liquid in the pores. The vapor velocity for a given heat flux $u_v = q_w/\rho_v h_{fg}$ can be used to calculate the vapor pressure drop in the thickness direction, along with the boundary condition $P_v = P_{sat}$ at $z = t$, to obtain

$$P_v(z) = P_{sat} + \left(\frac{\mu_v q_w}{KK_{rv}\rho_v h_{fg}} + \frac{C_E q_w^2}{K^{1/2} K_{rv} \rho_v h_{fg}^2} \right)(t - z) \tag{10}$$

An average vapor pressure (averaged over the z-direction) is obtained as

$$P_{v,avg} = P_{sat} + \left(\frac{\mu_v q_w}{KK_{rv}\rho_v h_{fg}} + \frac{C_E q_w^2}{K^{1/2} K_{rv} \rho_v h_{fg}^2} \right)\frac{t}{2} \tag{11}$$

The relative permeability for a given fluid combination can be a function of the intrinsic properties of the two fluids (such as the viscosity, interfacial tension, and contact angle) [25]. The widely used correlations for relative permeability in a porous medium consider it to be a function of the local liquid saturation s, which is the fraction of the porous volume filled with liquid. The relative permeability correlations for various macroscale porous media are found using techniques such as X-ray computed tomography (e.g., see ref. [26]) to measure the liquid saturation directly during two-phase flow through the medium. For microscale porous media, relative permeability correlations are obtained using indirect methods, such as weighing the sample to find the liquid saturation after testing (e.g., see ref. [27] for porous media used in fuel cells). Due to a lack of experimental measurements of relative permeability for microscale porous evaporators, some prior works on capillary-fed boiling have used fitted expressions for relative permeability from experimental measurements of dryout heat flux. At the dryout heat flux, it is known that the pressure drop from liquid flow through the evaporator region equals the maximum (available) capillary pressure. Cai and Bhunia [8] fitted the relative areas available for liquid and vapor flows to match their experimental predictions. Zhang *et al*. [28] used a fit for the vapor relative permeability, which was taken as a fraction of the intrinsic permeability of the copper inverse opal (CIO) evaporator

wick. In the absence of a universal correlation for relative permeability, we consider in this study the most general single-exponent power law expression for relative permeability [22, 23], respectively given for the liquid and vapor as

$$\begin{aligned} K_{rl} &= s^n \\ K_{rv} &= (1-s)^n \end{aligned} \tag{12}$$

The capillary pressure of the wick is the local difference between the average vapor and liquid pressures ($P_c = P_{v,avg} - P_l$). Similar to the relative permeability expression, the capillary pressure of a porous medium is modeled as a function of the local liquid saturation in multiphase flow as,

$$\begin{aligned} P_c(s) &= P_{c.\max} f(s) \\ &= \frac{2\sigma}{r_{eff}} f(s) \end{aligned} \tag{13}$$

where $P_{c,max}$ is the maximum capillary pressure of the porous medium, r_{eff} is the effective pore radius, σ is the surface tension of the fluid, and $f(s)$ characterizes the functional dependence on liquid saturation. When the porous medium is fully saturated, the capillary pressure is at its lowest. When liquid saturation decreases (i.e., as more vapor phase intrudes into the liquid saturated pore space), the capillary pressure increases. The capillary pressure function $f(s)$ for a given porous medium and fluid combination is typically found either by experimental measurements [29] or using pore-scale modeling and simulations [30]. Commonly used expressions for capillary-pressure saturation functions were tabulated by Kaviany [23]. In the absence of a universal capillary pressure-saturation relationship for microscale porous media, we consider a simple linear relationship $f(s) = 1 - s$ for the capillary pressure function.

Because the liquid and vapor pressures are functions of the radial coordinate, the capillary pressure ($P_c = P_{v,avg} - P_l$) and thereby the liquid saturation s, as well as relative permeabilities K_{rl} and K_{rv}, are all functions of the radial coordinate. The relative permeability of the liquid from equation (12) is substituted into equation (8) and using $P_c = P_{v,avg} - P_l$ gives,

$$\frac{dP_{v,avg}(s)}{dr} - \frac{dP_c(s)}{dr} = \frac{\mu_l}{K\left[s(r)\right]^n} G_w + \frac{\rho_l C_E}{K^{1/2}\left[s(r)\right]^n} G_w^{\,2} \tag{14}$$

where $G_w = q_w r/(2 \rho_l h_{fg} t)$. Substituting the average vapor pressure from equation (11), the capillary pressure from equation (13), and rearranging the terms, we arrive at a differential equation for the liquid saturation (s) as a function of radial coordinate,

$$\frac{ds(r)}{dr} = \frac{\left[\frac{\mu_l}{K\left[s(r)\right]^n} G_w + \frac{\rho_l C_E}{K^{1/2}\left[s(r)\right]^n} G_w^{\,2}\right]}{\left[\left(\frac{\mu_v q_w t}{2K\rho_v h_{fg}} + \frac{C_E q_w^{\,2} t}{2K^{1/2}\rho_v h_{fg}^{\,2}}\right)\frac{n}{\left[1-s(r)\right]^{n+1}} + P_{c,\max}\right]} \tag{15}$$

The equation is solved using a numerical stepping procedure, where the gradient ds/dr is calculated from the edge of the solution domain, with a known boundary condition (s ($r = r_e$) = s_e). The boundary condition s_e is found from the average vapor pressure and the known value of liquid pressure at the boundary ($P_l = P_{sat}$) using $P_{v,avg}\big|_{r=r_e} - P_l\big|_{r=r_e} = P_c\big|_{r=r_e}$ as,

$$\left(\frac{\mu_v q_w t}{2K\rho_v h_{fg}} + \frac{C_E q_w^{\,2} t}{2K^{1/2}\rho_v h_{fg}^{\,2}}\right)\frac{1}{(1-s_e)^n} = P_{c,\max}(1-s_e) \tag{16}$$

which provides,

$$s_e = 1 - \left(\frac{\mu_v q_w t}{2K\rho_v h_{fg} P_{c,\max}} + \frac{C_E q_w^{\,2} t}{2K^{1/2}\rho_v h_{fg}^{\,2} P_{c,\max}}\right)^{\frac{1}{n+1}} \tag{17}$$

Once the saturation profile $s(r)$ is obtained, the relative permeabilities can be found. From the vapor pressure and the capillary pressures (equations (11) and (13)), the liquid pressure profile can be obtained as,

$$P_l(r) = P_{sat} + \left(\frac{\mu_v q_w t}{2K\rho_v h_{fg}} + \frac{C_E q_w^{\,2} t}{2K^{1/2}\rho_v h_{fg}^{\,2}}\right)\frac{1}{\left(1-s(r)\right)^n} - P_{c,\max}\left(1-s(r)\right) \tag{18}$$

Dryout is considered to occur when the liquid saturation falls to zero at the center of the evaporator ($s(r = 0) = 0$). To find the dryout heat flux, equation (15) is solved using a definite integral with two known boundary conditions (s ($r = r_e$) = s_e and $s(r = 0) = 0$). From equation (15), substituting $q_w = q_{dry}$ we obtain,

$$\int_{s_e}^{0} s^n \left[n\frac{\left(Aq_{dry} + Bq_{dry}^{\,2}\right)}{\left[1-s\right]^{n+1}} + C\right] ds = \int_{r_e}^{0}\left[Dq_{dry} r + Eq_{dry}^{\,2} r^2\right] dr \tag{19}$$

where $A = \mu_v t/(2K\rho_v h_{fg})$, $B = C_E\, t/(2K^{1/2}\rho_v h_{fg}^{\,2})$ $C = P_{c,max}$, $D = \mu_l/(2K\rho_l h_{fg} t)$, $E = C_E/(4K^{1/2}\rho_l h_{fg}^{\,2} t^2)$ are known constants for a given wick and working fluid combination.

For a given wick and working fluid, the solution method calculates the boundary value of liquid saturation (s_e) and value of integrals on each side of equation (19) (using numerical integration in MATLAB) sweeping over a range of many q_{dry} values with high resolution. The difference between the integrals is found for each value of heat flux, and that which provides the minimum error (which is also

ensured to be <1%) is deemed the dryout heat flux q_{dry}. The only unknown in the expression to calculate the dryout heat flux (from equation (19)) is the saturation exponent n in the relative permeability relation. This exponent is obtained by calibrating the model-predicted dryout heat fluxes to experimentally measured values for sintered particle wick structures (in section 5.2) and for other common wick structures in the literature (in section 5.3.2).

3 Experimental measurements of dryout heat flux and thermal resistance

We characterize the dryout heat flux and boiling thermal resistance of sintered particle evaporator wicks with different particle sizes and heater sizes to collect data for model calibration. Deionized (DI) water is used as the working fluid. The experimental apparatus and data reduction procedures are detailed thoroughly in our prior work [6]; only critical information is briefly summarized here.

The capillary-fed boiling test setup allows the working fluid to be uniformly drawn into the evaporator from all directions and evaporate into the vapor space above that is maintained at saturation conditions (T_{sat} = 373 K, P_{sat} = 1 atm), as shown schematically in Figure 3. The heat input to the evaporator is provided using heater blocks (with embedded cartridge heaters) with two different contact areas of 5 mm × 5 mm and 10 mm × 10 mm. Copper particles of three different sizes (45 – 53 µm, 90 – 106 µm and 180 – 212 µm) and 1.5 mm thickness, are sintered onto solid copper substrates (38.1 mm × 38.1 mm dimension). The copper substrates with the evaporator wicks are then soldered to the copper block. The evaporator wicks are sealed using a novel dam structure to prevent liquid from flooding over the top. The open area for evaporation is 10 mm × 10 mm for both the heater sizes (see Figure 3).

Prior to each test, the copper wick is functionalized to be hydrophilic by dipping in a solution of 2M NaOH and 0.1M $(NH_4)_2S_2O_8$, rinsed in DI water, dried thoroughly with compressed nitrogen, and sealed into the chamber [6]. To obtain a boiling curve, heat input to the sample is turned on and increased in steps; the system is allowed to reach steady state at each step and thermocouple readings recorded. The heat flux into the wick (q_w) is calculated from a linear fit to a rake of thermocouple readings in the heater block; the wick base temperature is calculated by extrapolating from the thermocouple reading immediately below the substrate. The thermal resistance of the evaporator is then calculated as the ratio of the wick superheat to the heat input ($R_{th,wick} = (T_w - T_{sat})/(q_w A_{heater})$) where T_w is the wick base temperature and A_{heater} is the heater area. The heat flux is increased in steps until the occurrence of dryout is observed, signaled by a sudden and sharp increase in the wick base temperature.

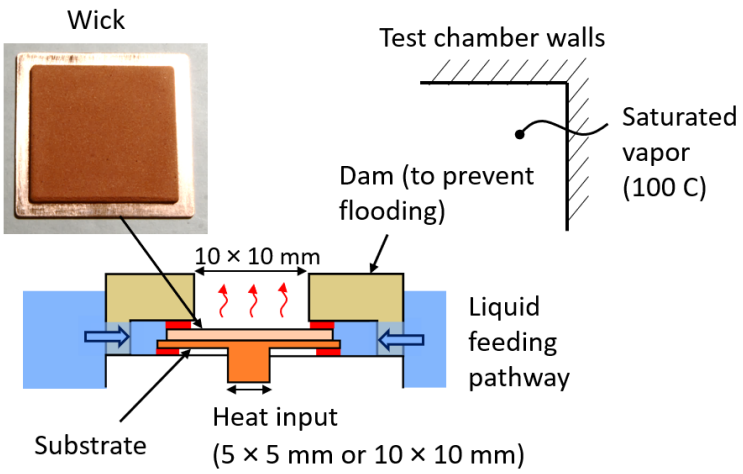

Figure 3. A schematic diagram illustrating the heating and liquid feeding mechanism for the evaporator wick, within the saturated test chamber. The inset image shows a photograph of a sample 90 – 106 µm particle wick structure. The reader is referred to Ref. [6] for more details on the capillary-fed boiling test facility. (note to editor: 1 column wide).

4 Illustration of model predictions for an example case

This section utilizes an example case study to illustrate the key characteristics of the model predictions, as well as to explore the effect of the effective film thickness δ and saturation exponent n on the model predictions. Details of the porous evaporator wick and working fluid for this example simulation case are shown in Table 1. The working fluid is water (at 373 K saturation temperature). A 1 mm thick sintered particle wick of particle size D = 100 µm and porosity φ = 0.6 is used over a heated area of 1 cm^2. The permeability and effective pore radius of this sintered-particle wick can then be calculated using the standard expressions provided in the table.

Table 1. Properties of the working fluid and porous evaporator wick used in the example case simulation (properties are calculated at saturation temperature of 373 K).

Property	Value
Liquid density (ρ_l)	958.45 kg/m^3
Vapor density (ρ_v)	0.5952 kg/m^3
Liquid viscosity (μ_l)	2.82×10^{-4}
Vapor viscosity (μ_v)	1.22×10^{-5}
Latent heat of vaporization (h_{fg})	2.26×10^6 J/Kg
Surface tension (σ)	5.88×10^{-2} N/m
Wick thickness (t)	1 mm

Wick particle size (D)	100 µm
Wick porosity (φ)	0.6
Heater radius (r_e)	5.6 mm
Solid thermal conductivity (k_s)	387.5 W/mK
Effective pore radius (r_{eff})	0.21 D
Wick permeability (K)	$D^2\varphi^3/450(1-\varphi)^2$
Effective thermal conductivity of wick (k_{eff})	$k_{eff} = (2-3\varphi)k_s/2$

Figure 4 (a) shows the model-predicted liquid saturation profiles along the radial direction (as calculated from equation (15)), for the example case at increasing values of heat flux. In this figure, the value of the saturation exponent is fixed at $n = 3$. At a heat flux of 25 W/cm^2, the liquid saturation does not vary much with the radial coordinate, and is nearly constant at its boundary value at $r = r_e$ (calculated from equation (17) as $s(r = r_e) = 0.71$). As the heat flux is increased, the magnitude of the liquid saturation decreases (due to the additional vapor generation in the evaporator). Further, the gradient along the radial direction increases, and the value of liquid saturation decreases from its boundary value toward the center of the domain (at $r = 0$). At $q_w = 378$ W/cm^2, the liquid saturation at the center of the domain reaches a value of zero, which signals the occurrence of dryout at this heat flux.

Figure 4 (b) plots the pressure profiles along the radial direction at the dryout heat flux value of $q_w = 378$ W/cm^2. The orange dash-dot curve shows the relative liquid pressure $P_l - P_{sat}$ as calculated from equation (18). The value reduces from zero at the outer edge of the evaporator to its minimum value at the center of the domain. The average excess vapor pressure $P_{v,avg} - P_{sat}$ reduces from the edge to the center, as shown by the blue curve. Since the liquid saturation reduces from the edge to the center, the relative permeability ($K_{rv} = (1 - s)^3$) and area available for vapor flow increases, and thus the average excess vapor pressure in the wick reduces (in the radially inward direction). Here, we note that the vapor temperature rise above saturation T_{sat} due to the excess vapor pressure would be negligible, thereby validating the assumptions made in the development of the thermal resistance model. Using the Clausius – Clapeyron relation ($dP/dT = h_{fg}P_{sat}/(R\,T_{sat}^2)$), the temperature rise for the maximum excess vapor pressure (~ 3200 Pa at the edge of the evaporator) is ~ 0.02 K. The capillary pressure of the wick (difference between the average vapor pressure and the liquid pressure) is lowest at the outer edge and highest at the center of the domain (at $r = 0$), where the liquid saturation is the lowest. At this dryout heat flux, the capillary pressure at the center of the domain becomes equal to the maximum available capillary pressure $P_{c,max}$ of the wick indicated by the dashed horizontal reference line in Figure 4 (b).

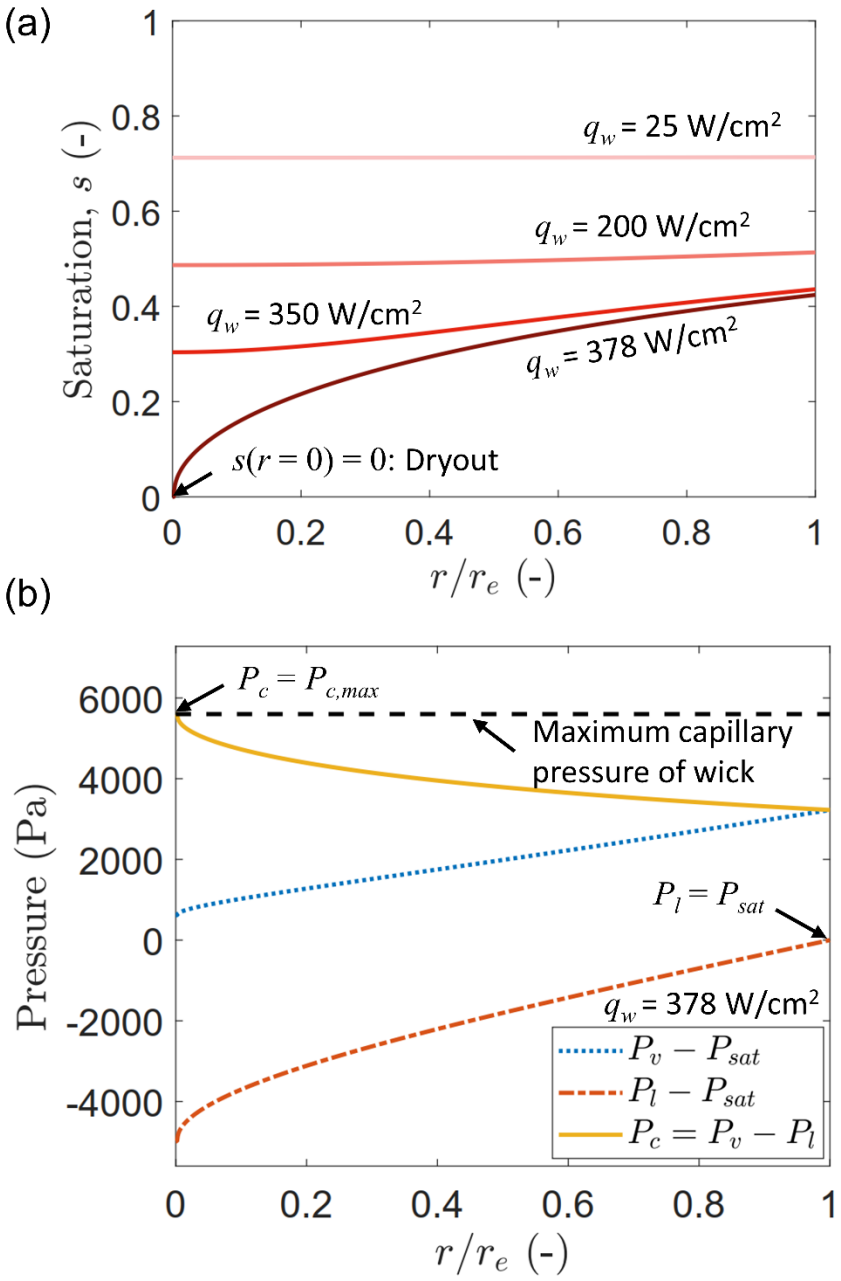

Figure 4. (a) A plot of the liquid saturation s as a function of the normalized radial coordinate r/r_e for the example case (refer Table 1 for properties) at different heat fluxes, calculated using the saturation exponent value n = 3. At q_w = 378 W/cm^2, dryout is indicated by the value of liquid saturation falling to zero at the center of the domain ($s(r = 0)=0$). (b) A plot of the liquid, average vapor, and capillary pressures as a function of the radial coordinate at the dryout heat flux (q_w = 378 W/cm^2). (note to editor: 1 column wide).

To illustrate the dependence of the dryout heat flux predicted by the model on the saturation exponent n, Figure 5 shows the liquid saturation at the center of the evaporator domain ($s(r = 0)$) as a function of the heat flux for different values of the saturation exponent. As seen in the plot, the saturation value decreases with increasing heat flux from $s = 1$ (at no heat input) to the dryout heat flux ($q_w = 378$ W/cm^2) at which $s(r = 0)=0$. The liquid saturation value, at any given value of n, exhibits a steep fall to zero as the heat fluxes approaches the dryout value. For example, in the orange solid curve, the saturation value falls from $s \approx 0.3$ to $s = 0$ from $q_w = 183$ W/cm^2 to 191 W/cm^2. Since the liquid relative permeability scales as $K_l \sim s^n$, any reduction in the liquid saturation causes a much steeper reduction in the liquid permeability, which causes a higher drop in the liquid pressure and a subsequent rise in the capillary pressure. This further exacerbates the reduction in the liquid saturation, and hence causes this steep change close to the dryout heat flux. The dryout heat flux predicted by the model reduces from 378 W/cm^2 to 95 W/cm^2 as the exponent is increased from $n = 3$ to $n = 5$. This is primarily due to the decrease in the liquid relative permeability as the exponent value is increased, which contributes to a higher pressure drop and a steeper reduction in liquid saturation (with increasing heat fluxes), and thus a lower dryout heat flux.

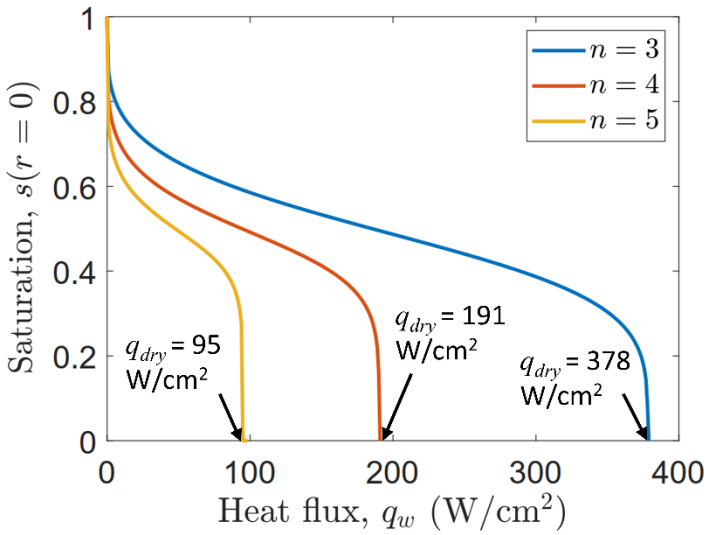

Figure 5. A plot of the liquid saturation at the center of the wick domain ($s(r = 0)$) as a function of the applied heat flux q_w for different values of the saturation exponent n for the example case (refer to Table 1 for properties). The values of the dryout heat flux at which ($s(r = 0)=0$) are labelled. (note to editor: 1 column wide)

Figure 6 shows the model-predicted solid superheat ($\theta_s = T_s - T_{sat}$) along the thickness of the wick (z direction), at an input heat flux of $q_w = 100$ W/cm^2, for different effective film thicknesses δ. The superheat is highest at the base of the wick and decreases to its minimum value at the top of the wick exposed to the saturated vapor. The boiling resistance predicted by the model is calculated using equation (6) based on the

total temperature drop across the evaporator thickness. The plot also reveals the dependence of the wick superheat magnitude and profile on δ/r_{eff} (*i.e.*, the effective film thickness as a fraction of the effective pore radius of the wick). Following the pore-scale evaporation model outlined in Appendix A, at higher effective film thicknesses, the thermal resistance is dominated by conduction across the liquid film. This leads to a larger solid superheat and thus a larger boiling resistance for larger effective film thicknesses. The superheat profiles are analogous to 1D conduction heat transfer across a solid fin, with different effective thermal resistances to heat transfer from the surface of the fin. The maximum wick superheat ranges from θ_s = ~ 5 to 34 °C for film thickness ratio ranging from δ/r_{eff} = 0.1 to 0.95, which corresponds to a boiling resistance per unit area for this example case from R_{th} = 0.05 to 0.34 K cm^2/W. Note that for a given wick geometry and working fluid combination, and at a given effective film thickness, the model predicts that the boiling resistance per unit area (in K m^2/W) is a constant value, and not a function of the heat input.

As seen in Figure 5 and Figure 6, the model-predicted values of the dryout heat flux and thermal resistance are sensitive to the unknown parameters (namely, the saturation exponent *n* and the film thickness ratio δ/r_{eff}). This result signifies the importance of calibrating these unknown parameters with experimental data on different evaporator wick structures in order to adopt the model for more general use, as is explored next in Section 5. We survey calibration against a broad set of data to evaluate if a single value of the parameters can be used against the whole set of data.

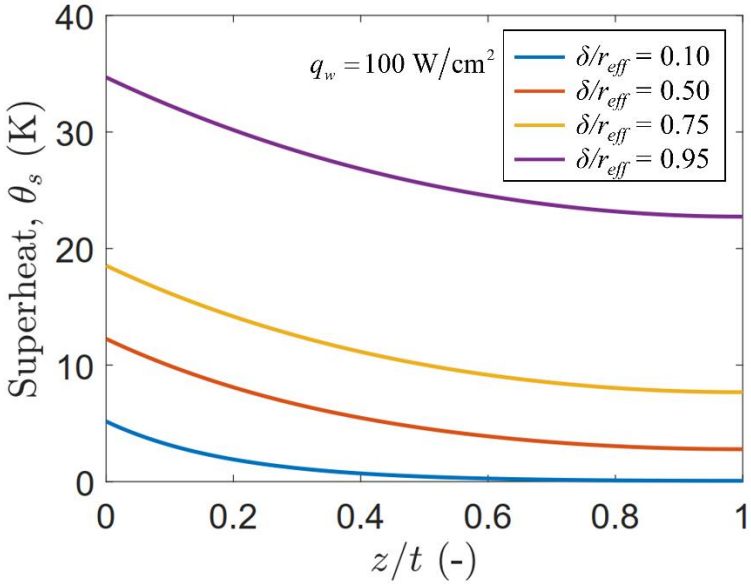

Figure 6. (a) A plot of the superheat of the solid matrix ($\theta_s = T_s - T_{sat}$) along the z-direction for different values of the film thickness ratio δ/r_{eff} for the example case (refer Table 1 for properties). (note to editor: 1 column wide).

5 Model calibration

The model developed in this work is calibrated against a wide range of data for different types of porous evaporators. The model unknowns, namely the effective film thickness δ and the saturation exponent n are fit to experimental measurements of thermal resistance and dryout heat flux, respectively. We focus on the most commonly used porous structures for loop heat pipes and vapor chambers, namely, sintered particle, sintered screen mesh, and micro-pillared structures. The inputs to the model are the effective properties of the evaporator wick structure (as will be described in the next subsection), and the thermophysical properties of the working fluid. The model calibration to experimental results for sintered particle wicks obtained in the current work is then presented, followed by calibration to data collected from the literature.

5.1 Evaluation of effective porous media properties

Table 2 lists expressions for the effective properties of the three different wick structures, namely sintered particles, sintered screen mesh, and micro-pillars.

For sintered copper particle wick structures, Bodla *et al.* [31] showed that the expression for effective thermal conductivity of the wick k_{eff} derived from effective medium theory (EMT) provided the best comparison to calculations from numerical simulations of heat conduction through geometrically faithful reconstructions of sintered particle wicks. The expression from EMT is:

$$k_{eff} = \frac{1}{4}\left[\left(3\varphi-1\right)k_l + \left[3\left(1-\varphi\right)-1\right]k_s + \sqrt{\left[\left(3\varphi-1\right)k_l + \left(3\left(1-\varphi\right)-1\right)k_s\right]^2 + 8k_l k_s}\right] \tag{20}$$

The expression can be simplified for a copper particle – water combination by enforcing $k_l << k_s$ to:

$$k_{eff} = \frac{\left(2-3\varphi\right)}{2}k_s \tag{21}$$

The effective pore radius of sintered particle wicks is recommended as $r_{eff} = 0.21\ D$ by Faghri [32] and is used in the current work. The intrinsic permeability of sintered particle structures is typically considered as $K = d^2\varphi^3/150(1-\varphi)^2$ [34]. However, Bodla *et al.* [31] found that the values calculated from single-phase flow simulations in sintered particle structures were 3 times lower than the ones calculated from this expression, and instead recommended $K = d^2\varphi^3/450(1-\varphi)^2$.

For sintered screen mesh wick structures, a number of studies proposed thermal conductivity correlations based on their own experiments, e.g., Refs. [33,34]. We use an expression provided by Li and Peterson [35] based on a correlation to experimental measurements obtained from staggered screen mesh wick structures of different mesh numbers and number of layers,

$$k_{eff} = 1.42\frac{k_s\left(M\times d\right)^2}{t}2n_{layer}d \tag{22}$$

where M is the mesh number and n_{layer} is the number of layers. The commonly recommended effective pore radius of screen mesh wicks is $r_{eff} = (W+d)/2$ [7,32] where d is the diameter of the screen mesh wire, and W is the width of the screen mesh pore. The intrinsic permeability is calculated as $K = d^2\varphi^3/122(1-\varphi)^2$ following Faghri [34].

Micro-pillared wick structures have been recently utilized in various thin-film evaporation applications [36]. They are best suited for usage in flexible polymer-based heat pipes [37] or titanium heat pipes [38]. We use the values of effective pore radius $r_{eff} = d/2(1-\varphi)$, effective thermal conductivity calculated from a parallel resistance network for thermal conduction through the micro-pillar structure $k_{eff} = k_s(1-\varphi)$ and intrinsic permeability $K = d^2\varphi^3/50\,(1-\varphi)^2$ as recommended by Cai and Bhunia [8,9].

Table 2. Relations for the intrinsic permeability (K), effective thermal conductivity (k_{eff}), and effective pore radius (r_{eff}) for three commonly used evaporator wick structures.

Wick Type	**Wick Permeability (K)**	**Effective thermal conductivity (k_{eff})**	**Effective pore radius (r_{eff})**
Sintered particles	$K = \frac{D^2\phi^3}{450(1-\phi)^2}$	$k_{eff} = \frac{(2-3\varphi)k_s}{2}$	$r_{eff} = 0.21D$
Sintered screen mesh	$K = \frac{d^2\phi^3}{122(1-\phi)^2}$	$k_{eff} = 1.42\frac{k_s(Md)^2}{t/2n_{layer}d}$	$r_{eff} = \frac{(W+d)}{2}$
Micro-pillars	$K = \frac{d^2\phi^3}{50(1-\phi)^2}$	$k_{eff} = k_s(1-\varphi)$	$r_{eff} = \frac{d}{2(1-\phi)}$

5.2 Model calibration against sintered wick experimental results

Table 3 shows the measured dryout heat flux and the average boiling thermal resistance of the sintered particle evaporator wicks that were tested in the current work, at each heater size. The dryout heat flux increases with particle size and is highest for the 180 – 212 µm wick structures, with a value of 191 W/cm^2 and 793 W/cm^2 for the 10 mm × 10 mm and 5 mm × 5 mm heater sizes, respectively. Furthermore, the dryout heat fluxes are higher for smaller heater areas; the significantly higher values for the 5 mm × 5 mm heater are due to the reduced flow length and pressure drop for liquid feeding over the smaller area. The reader is referred to Appendix B for the full boiling curve and thermal resistance curves plotted against the heat flux, and for the uncertainties in the measured values. In this section, the model is calibrated against the experiments by fitting for the film thickness ratio δ/r_{eff} and the saturation exponent n in the relative permeability expression.

Table 3. Measured dryout heat flux and boiling thermal resistance of the wick structures at two different heater sizes.

Particle size (μm)	Heater size (mm × mm)	Dryout heat flux (W/cm^2)	Average boiling resistance (K/W)
45-53	5 × 5	247	0.111
	10 × 10	83	0.083
90-106	5 × 5	287	0.117
	10 × 10	104	0.106
180-212	5 × 5	793	0.110
	10 × 10	191	0.157

Figure 7 shows a comparison of the predicted and experimental heat flux values for the three different particle sizes. The predicted heat flux q_{model} is calculated by dividing the measured wick superheat (at a measured heat flux) by the predicted boiling resistance (R_{th}, given by equation (6), as $q_{model} = \Delta T_{wick}/R_{th}$). The film thickness ratio δ/r_{eff} is assumed to be unique for a given wick particle size and therefore fitted separately for each particle size. Values of $\delta/r_{eff} = 0.76$ (for 45 – 53 μm particles), $\delta/r_{eff} = 0.48$ (for 90 – 106 μm), and $\delta/r_{eff} = 0.27$ (for 180 – 212 μm) provide the lowest least-squared error between the predicted and experimental heat fluxes. The experimental data are well-predicted within a spread of ±25% by the model across all particle sizes, heater areas, and superheats. Interestingly, the values of fitted film thickness ratio δ/r_{eff}, which reduce from 0.76 to 0.27 as the particle size increases, correspond to a relatively unchanged absolute value of effective film thickness (within a range between ~8-11 μm) across the different particle sizes.

Figure 8 shows a comparison of the predicted and experimentally measured dryout heat fluxes for all the test cases. The saturation exponent n in the relative permeability expression is again fitted uniquely for each evaporator wick particle size (but held constant across the different heater areas). A higher value of the relative permeability exponent means that the relative permeability of liquid is lower for the same value of liquid saturation and suggests a higher liquid feeding pressure drop penalty imposed by boiling. The best-fit values of $n = 3.9$ (for 45 – 53 μm particles), $n = 4.7$ (90 – 106 μm), and $n = 4.4$ (180 – 212 μm) yield the minimum RMS error between the model predictions and experimental measurements. All the data are captured within a spread of ± 15%. The experimentally measured dryout heat flux values depend primarily on the particle size of the evaporator wick and the heater area. For larger particle sizes, the liquid feeding pressure drop from the sides of the evaporator will be lower due to a higher absolute permeability. Although the capillary pressure is lower for larger particle sizes ($P_{c,max} \sim 1/D$), the effect of the larger absolute permeability ($K \sim D^2$) outweighs the lower capillary pressure for this particle size range. The dryout

heat fluxes are 3-4 times higher for the smaller heater size compared to the larger heater size, and this critical effect is well captured by the model for all the particle sizes as evidenced by Figure 8. Other prior works on capillary-fed boiling have also demonstrated the critical effect of heater size on the measured dryout heat fluxes [9,18]. The overall trends in particle size and heater size are predicted well by the model despite the small variation in the fitted exponent value (n = 3.9 – 4.7).

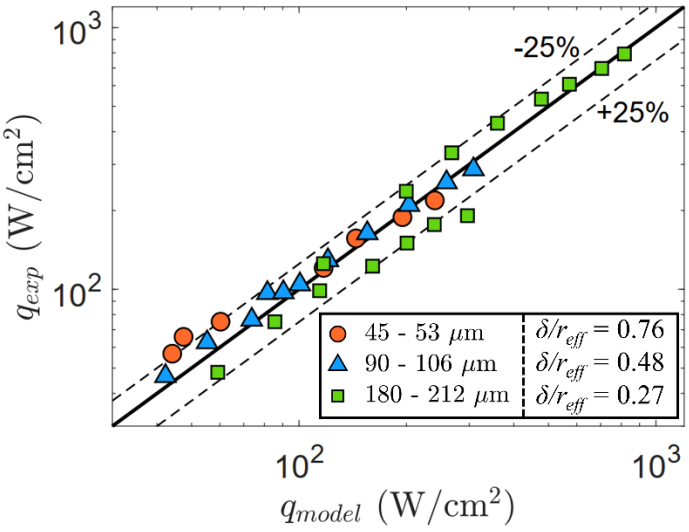

Figure 7. Comparison of the predicted and experimentally measured heat fluxes at a given superheat. (note to editor: 1 column wide)

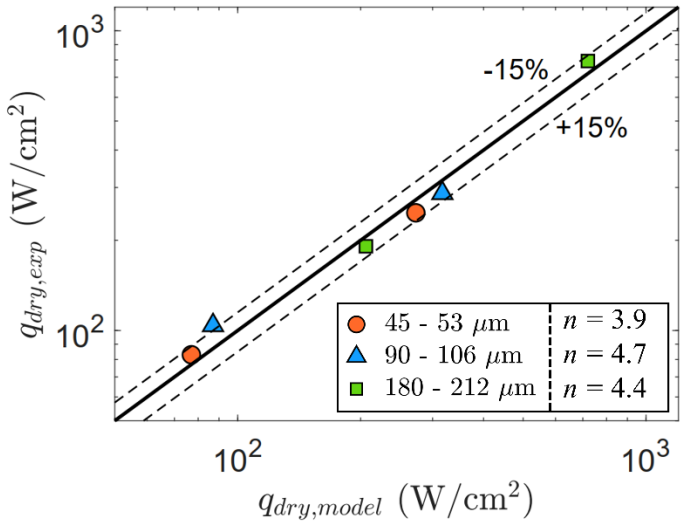

Figure 8. Comparison of the predicted and experimentally measured dryout heat fluxes (the two different values of dryout heat flux for each particle size correspond to the two different heater sizes). (note to editor: 1 column wide)

5.3 Model calibration against data from the literature

5.3.1 Thermal resistance calibration

Results from three studies in the literature for the three different wick structures are used in the calibration, all using water at 373 K saturation temperature (see Table 1 for properties) as the working fluid. The effective wick thermal conductivity and pore radius from Table 2 are used in the model.

Weibel *et al.* [39] characterized sintered particle evaporator wick structures (255 – 355 μm; r_{eff} = 0.21; D = 63 μm) of thicknesses ranging from 600 – 1200 μm. The measured substrate superheat is used to predict the heat flux q_{model} fitting the film thickness ratio (δ/r_{eff} = 0.1) so that the RMS error between q_{exp} and q_{model} is the lowest. Li and Peterson [41] tested multiple layers of sintered screen mesh wick structures (mesh number M = 5709 m^{-1}, d = 56 μm, W = 119 μm, r_{eff} = 87.5 μm), with the screen meshes placed in a staggered orientation. The boiling curve data for three different thicknesses t = 370, 570 and 740 μm (n_{layer} = 4, 6 and 8) are used here for model calibration by finding the best fit (δ/r_{eff} = 0.1) to this group of experimental data. Cai and Bhunia [8] obtained boiling curves for monoporous silicon micro-pillar wicks of pillar diameter d = 100 μm, at two different thicknesses of 220 μm and 320 μm. The film thickness ratio obtained for these results is δ/r_{eff} = 0.01.

Figure 9 shows the calibration data q_{exp} plotted against q_{model} for the three different sets of results [8,39,41]. The predicted values q_{model} are calculated from the measured superheat values, using the predicted thermal resistance (R_{th}, given by equation (6)), as $q_{model} = \Delta T_{wick}/R_{th}$. A majority of the predicted values >100 W/cm^2 fall within ±25% of the experimental data, for a wide range of heat fluxes from 100 – 1000 W/cm^2. This suggests a good correlation between the predicted and experimental values of thermal resistance, based on the different (fitted) film thickness ratios for different types of wicks. The deviation from the predicted values at heat fluxes less than 100 W/cm^2 is primarily due to evaporation-dominated heat transfer in the wick (prior to the onset of nucleate boiling) at lower heat fluxes. The absolute value of the fitted film thickness is on the same order of magnitude across the different wick structures (δ = 6.3 μm, 8.75 μm and 1.25 μm for the sintered particles, sintered screen mesh, and silicon micro-pillar structures, respectively).

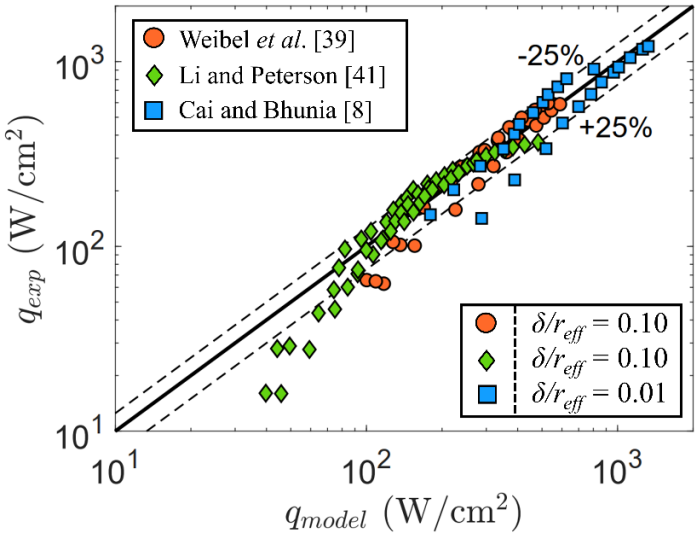

Figure 9. Comparison of the predicted and experimentally measured heat fluxes from three different evaporator wick structures in the literature: sintered particle [39], sintered screen mesh [41] and micro-pillar structures [8]. (note to editor: 1 column wide)

5.3.2 Dryout heat flux model calibration

Dryout heat flux data from the literature on a wide variety of wick structures (water at 373 K saturation temperature is the working fluid), with different thickness, particle/pore sizes and heater areas are used in calibrating the model for dryout heat flux. The working fluid properties in Table 1 and the intrinsic wick permeability from Table 2 are inputs to the model in calculating the predicted dryout heat flux. Figure 10 shows a comparison between the model and the experimentally measured values. A single saturation coefficient (n = 4.0) is fit across all the predicted values, a majority of which fall within ± 25% of the experimental values across a wide variety of evaporator designs (with a mean absolute percentage error (MAPE) of 33%). This strong correlation between the model and experiment obtained using a single saturation coefficient demonstrates that the model captures well the widely accepted trends in the literature including the effects of wick thickness, pore size, and heater size. These key trends from the literature, and the corresponding model predictions are explained here.

The increase in dryout heat flux with increase in particle/pore size has been experimentally observed across all three wick structures. Li and Peterson [7] tested the effect of pore size on the dryout heat flux of screen mesh wicks using three different screen mesh openings (W = 119.3 µm, W = 139.7 µm, W = 232.8 µm) and found that the dryout heat flux increases with increase in mesh opening size. This was attributed to the increase in wick permeability. Cai and Bhunia [9] tested silicon micro-pillar wick structures of two

different pillar diameters (30 µm and 100 µm) and found that the dryout heat flux increases with pillar diameter. In our recent work [18] and in the current paper, this same trend is observed with increase in particle size (45 – 53 µm, 90 – 106 µm and 180 – 212 µm), due to the increased permeability offered by the larger particles. Similarly, Li and Peterson [41] concluded that increasing the wick thickness from 0.37 mm to 0.74 mm (by stacking multiple layers of sintered screens) improves the dryout heat flux by providing more cross-sectional area for liquid replenishment. Cai and Bhunia [8] found that increasing the pillar height from 220 µm to 320 µm enhances the dryout heat flux. Further, the critical effect of heater size on dryout heat flux was demonstrated by Weibel [40] and also in the current paper (using 5 mm × 5 mm and 10 mm × 10 mm heaters) and by Cai and Bhunia [8] (using 2 mm × 2 mm and 10 mm × 10 mm heaters).

The model is able to capture the key trends of increasing dryout heat flux with increasing the characteristic particle/pore size, increasing wick thickness, and decreasing heater area, using a single saturation exponent value of $n = 4.0$ across the entire dataset ranging over nearly three orders of magnitude of dryout heat flux. This provides confidence that the capillary-fed boiling model developed here can be utilized to predict the dryout limit across a wide variety of evaporator wick geometries and properties.

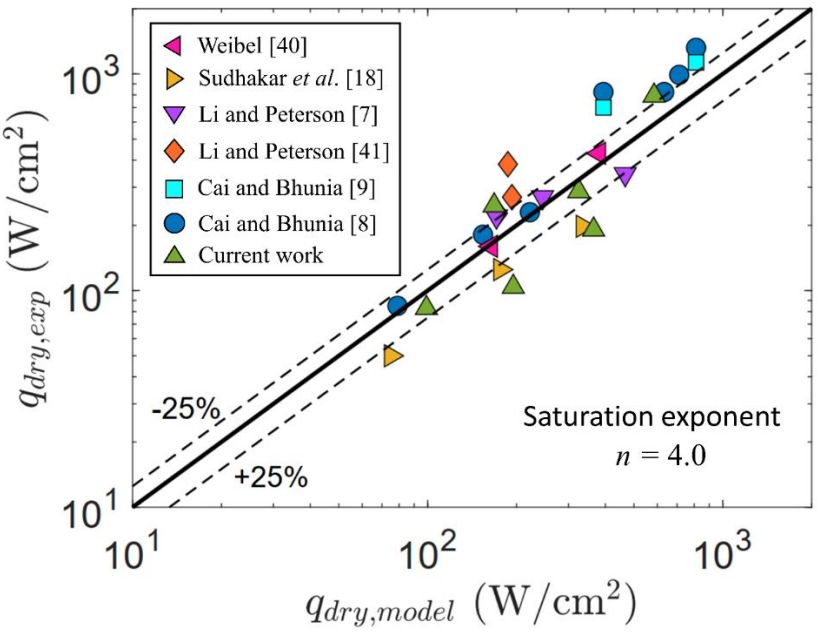

Figure 10. A comparison of the experimentally measured values of dryout heat flux from the literature and predicted values from the model developed in this study. The comparison includes data on sintered particle wicks from Weibel [40] and Sudhakar *et al.* [18], sintered screen mesh wick structures from Li and Peterson [7,41], and micro-pillar wick structures from Cai and Bhunia [8,9]. (note to editor: 1 column wide)

6 Conclusions

This paper developed a new thermofluidic model for the prediction of the dryout heat flux limit and thermal resistance during capillary-fed boiling in porous evaporators used in two-phase heat transport devices such as vapor chambers, loop heat pipes, and capillary pumped loops. The modeling of multi-phase flow within porous media relies on the availability of constitutive relationships for the relative permeability as a function of the liquid saturation. Hence, two-phase flow models typically utilize correlations based on experimental measurements of relative permeability that are only largely available for macroscale porous beds, and not for microscale capillary-fed porous evaporators in the flow configuration studied herein. The semi-empirical modeling framework presented in this work is developed for prediction of dryout heat flux and thermal resistance in these scenarios. In the model, conduction and evaporation heat transfer in the porous medium are solved for to obtain the boiling thermal resistance. Lateral liquid flow from the edge to the center of the evaporator and vapor flow across the thickness are modeled to obtain the local liquid and vapor pressures. The input heat flux at which the liquid saturation at the center of the evaporator falls to zero is defined as the dryout limit. Experiments were performed using sintered particle evaporators of different particle and heater sizes and the data was used for model calibration. The model is also calibrated against experimental data collected from the literature on sintered particles, sintered screen meshes, and micro-pillar structures. For the thermal resistance, the model is calibrated against individual sets of data with an accuracy of ± 25%. It was found that the calibrated values of film thickness ratios for the thermal resistance model depend on the specific wick structure. The model also predicts the dryout limit of a wide variety of porous evaporators ranging across nearly three orders of magnitude with a mean absolute percentage error of 33% and captures the trends in particle/pore size, evaporator wick thickness and heater size. From this universal calibration, a single saturation exponent value of $n = 4.0$ is recommended for use in boiling in capillary-fed porous evaporators as it provided the best fit across different evaporator wick geometries and effective properties.

Appendix A. Pore-scale evaporation model

To obtain a volumetric heat transfer coefficient, a pore-scale evaporation model is developed as detailed below. The heat transfer in each pore (from the solid porous matrix to the vapor in the pore, as shown in Figure 2 (b) in the main text) occurs by conduction across the annular liquid film and evaporation from the liquid-vapor interface, as shown schematically in Figure A.1. The vapor phase in the pore is at T_{sat} and the liquid-vapor interface is at a constant temperature T_{lv}. The conduction flux across the annular liquid film is obtained as

$$q_{cond,l} = -k_l \frac{\left(T_s - T_{lv}\right)}{\left(r_{eff} - \delta\right)\ln\left(\frac{r_{eff} - \delta}{r_{eff}}\right)} \tag{A.1}$$

The pore-scale evaporation flux is

$$q_{evap,p} = h_{lv}\left(T_{lv} - T_{sat}\right) \tag{A.2}$$

where h_{lv} is the heat transfer coefficient for evaporation of liquid to vapor at a saturation temperature T_{sat} and pressure P_{sat} obtained from kinetic theory [42]

$$h_{lv} = \frac{2\sigma}{\left(2-\sigma\right)} \frac{{h_{fg}}^2}{T_{sat} v_{fg}} \left(\frac{1}{2\pi R T_{sat}}\right)^{1/2} \left(1 - \frac{P_{sat}}{2 v_{fg} h_{fg}}\right) \tag{A.3}$$

In the above expression, an accommodation coefficient of $\sigma = 0.03$ is used. The total heat transfer rate from each pore is obtained by integrating the evaporation flux over the open pore area,

$$Q_{pore} = 2\pi\left(r_{eff} - \delta\right) h_{lv}\left(T_{lv} - T_{sat}\right) t_{pore} \tag{A.4}$$

Equating the expressions in equations (A.1) and (A.2), and eliminating the liquid-vapor interface temperature variable T_{lv}, we obtain the expression for the total heat transfer from each pore,

$$Q_{pore} = 2\pi\left(r_{eff} - \delta\right) h_{lv} \frac{\left(T_s - T_{sat}\right) t_{pore}}{\left(1 + \frac{h_{lv}}{k_l}\left(r_{eff} - \delta\right)\ln\left(\frac{r_{eff}}{r_{eff} - \delta}\right)\right)} \tag{A.5}$$

The volumetric evaporation heat transfer rate in the control volume is calculated by summing the heat transfer across all the pores in the control volume per unit volume as

$$\tilde{q}_{evap} = \frac{Q_{pore} N}{V_{CV}} = \frac{2\left(r_{eff} - \delta\right) h_{lv} \varphi}{{r_{eff}}^2 \left(1 + \frac{h_{lv}}{k_l}\left(r_{eff} - \delta\right)\ln\left(\frac{r_{eff}}{r_{eff} - \delta}\right)\right)} \left(T_s - T_{sat}\right) \tag{A.6}$$

In the above equation, $V_{CV} = N.V_{pore}/\varphi$ where φ is the porosity of the wick and $V_{pore} = \pi r_{eff}^2 t_{pore}$ were utilized. Equating (A.6) to the expression for $\tilde{q}_{evap}$ from equation (1) in the main text, the volumetric heat transfer coefficient is obtained as,

$$\tilde{h}_{evap} = \frac{2\left(r_{eff} - \delta\right) h_{lv} \varphi}{r_{eff}^{\,2}\left(1 + \frac{h_{lv}}{k_l}\left(r_{eff} - \delta\right)\ln\left(\frac{r_{eff}}{r_{eff} - \delta}\right)\right)} \tag{A.7}$$

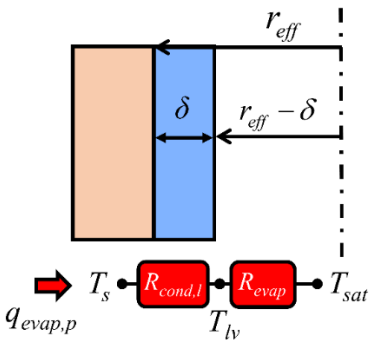

Figure A.1. A schematic diagram illustrating the pore-scale evaporation model, including the resistances for heat transfer by conduction across a thin liquid film and evaporation from the liquid-vapor interface.

Appendix B. Boiling curves for sintered particle wicks

Figure B.1 and Figure B.2 show the (a) boiling curve, *i.e.*, the input heat flux q_w plotted against the substrate superheat ΔT_{sub} and (b) thermal resistance ($R_{th,meas} = \Delta T_{sub}/ (q_w A_{heater})$) plotted against the input heat flux, for the three different particle size evaporator wicks with the 10 mm × 10 mm and 5 mm × 5 mm heater sizes, respectively. The highest heat flux value shown in the plots is the maximum heat flux sustained by the evaporator at steady state prior to dryout, which is the measured dryout heat flux of the sample. The complete data reduction and uncertainty calculation procedures are detailed in our prior work in Ref. [6].

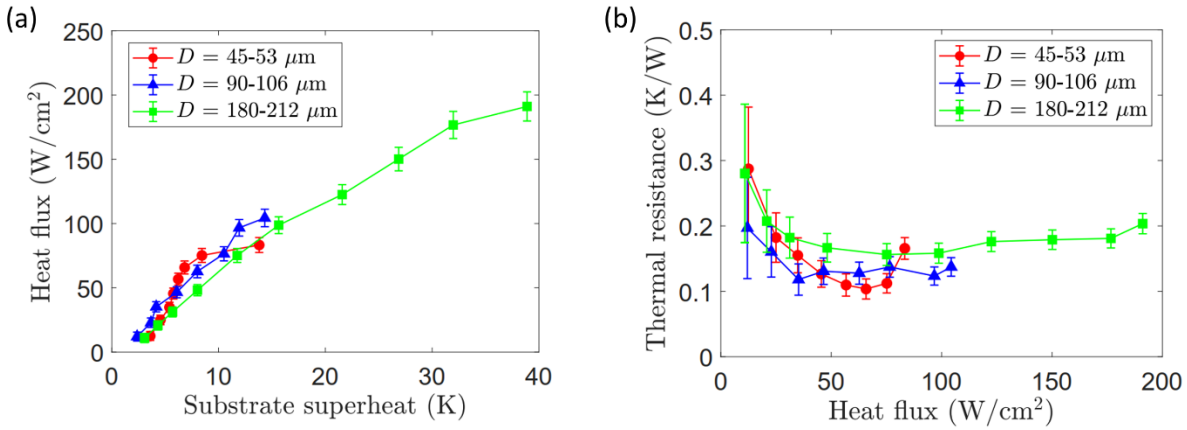

Figure B.1. (a) The input heat flux (q_w) plotted against the measured substrate superheat (ΔT_{sub}) and (b) the thermal resistance plotted against the input heat flux, for the three particle size evaporator wicks, for a heater size of 10 mm × 10 mm. Error bars in part (a) and (b) show the uncertainty in the measured heat flux and the thermal resistance, respectively. (note to editor: 2 columns wide)

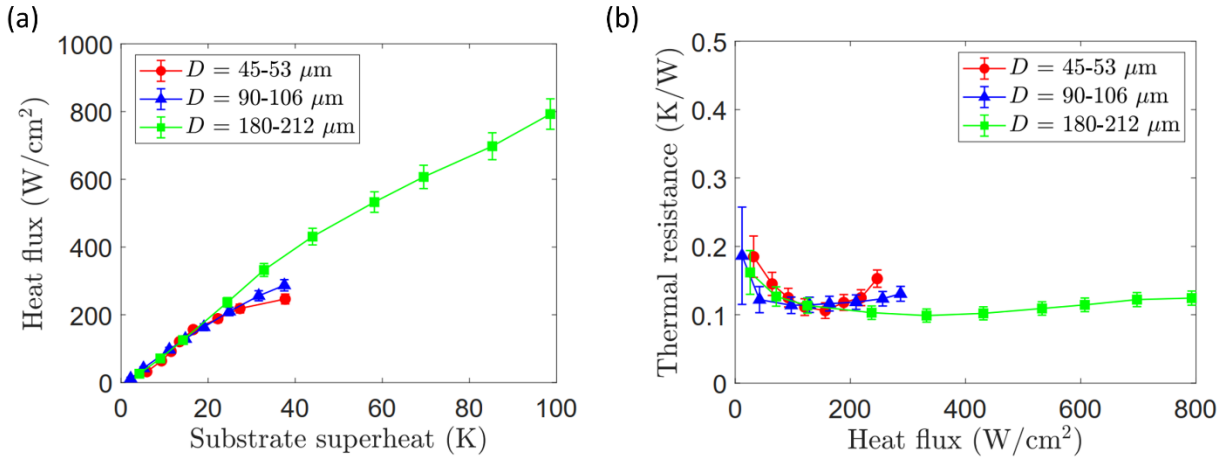

Figure B.2. (a) The input heat flux (q_w) plotted against the measured substrate superheat (ΔT_{sub}) and (b) the thermal resistance plotted against the input heat flux, for the three particle size evaporator wicks, for a heater size of 5 mm × 5 mm. Error bars in part (a) and (b) show the uncertainty in the measured heat flux and the thermal resistance, respectively. (note to editor: 2 columns wide)

To obtain the wick superheat, the temperature drop due to conduction resistance across the substrate is deduced from the measured substrate superheat as,

$$\Delta T_{wick} = \Delta T_{sub} - \frac{t_{sub}}{k_{Cu} A_{boil}} Q_w \tag{B.1}$$

where t_{sub} is the substrate thickness, k_{Cu} is the thermal conductivity of the copper substrate, A_{boil} is the boiling area (10 mm × 10 mm open area) and Q_w is the heat input. The average boiling resistance quoted in Table 3 is calculated by subtracting the 1D substrate conduction resistance from the measured thermal resistance, as shown below, and averaging over the measured values once the thermal resistance reaches a nearly constant value as a function of heat flux,

$$R_{th,wick} = R_{th,meas} - \frac{t_{sub}}{k_{Cu} A_{boil}} \tag{B.2}$$

References

[1] A. L. Moore and L. Shi, “Emerging challenges and materials for thermal management of electronics,” *Materials Today*, vol. 17, pp. 163–174, 2014.

[2] M. Bulut, S. G. Kandlikar, and N. Sozbir, “A review of vapor chambers,” *Heat Transfer Engineering*, vol. 0, pp. 1–23, 2018.

[3] X. Chen, H. Ye, X. Fan, T. Ren, and G. Zhang, “A review of small heat pipes for electronics,” *Applied Thermal Engineering*, vol. 96, pp. 1–17, 2016.

[4] A. Ambirajan, A. A. Adoni, J. S. Vaidya, A. A. Rajendran, D. Kumar, and P. Dutta, “Loop heat pipes: A review of fundamentals, operation, and design,” *Heat Transfer Engineering*, vol. 33, pp. 387–405, 2012.

[5] J. A. Weibel and S. V. Garimella, “Visualization of vapor formation regimes during capillary-fed boiling in sintered-powder heat pipe wicks,” *International Journal of Heat and Mass Transfer*, vol. 55, pp. 3498–3510, 2012.

[6] S. Sudhakar, J. A. Weibel, and S. V. Garimella, “Experimental investigation of boiling regimes in a capillary-fed two-layer evaporator wick,” *International Journal of Heat and Mass Transfer*, vol. 135, pp. 1335–1345, 2019.

[7] C. Li and G. P. Peterson, “Evaporation/Boiling in thin capillary wicks (II)—Effects of volumetric porosity and mesh size,” *Journal of Heat Transfer*, vol. 128, pp. 1320–1328, 2006.

[8] S. Q. Cai and A. Bhunia, “Geometrical effects of wick structures on the maximum phase change capability,” *International Journal of Heat and Mass Transfer*, vol. 79, pp. 981–988, 2014.

[9] S. Q. Cai and A. Bhunia, “Characterization of phase change heat and mass transfers in monoporous silicon wick structures,” *Journal of Heat Transfer*, vol. 136, p. 072001, 2014.

[10] C-Y. Wang and C. Beckermann, “A two-phase mixture model of liquid-gas flow and heat transfer in capillary porous media-l. Formulation,” *International Journal of Heat and Mass Transfer*, vol. 36, pp. 2747 – 2758, 1993.

[11] C. Figus, Y. L. Bray, S. Bories, and M. Prat, “Heat and mass transfer with phase change in aporous structure partially heated: continuum model andpore network simulations,” *International Journal of Heat and Mass Transfer*, vol. 42, pp. 2557–2569, 1999.

[12] M. Prat, “Pore network models for the study of transfers in the porous wick of loop heat pipes,” *Heat Pipe Science and Technology, An International Journal*, vol. 1, pp. 129–149, 2010.

[13] S. G. Liter and M. Kaviany, “Pool-boiling CHF enhancement by modulated porous-layer coating: theory and experiment,” *International Journal of Heat and Mass Transfer*, vol. 44, pp. 4287–4311, 2001.

[14] R. L. Webb, “Nucleate Boiling on Porous Coated Surfaces,” *Heat Transfer Engineering*, vol. 4, pp. 71–82, 1983.

[15] S. M. Rao and A. R. Balakrishnan, “Analysis of pool boiling heat transfer over porous surfaces,” *Heat and Mass Transfer*, vol. 32, pp. 463–469, 1997.

[16] J. Y. Chang and S. M. You, “Boiling heat transfer phenomena from microporous and porous surfaces in saturated FC-72,” *International Journal of Heat and Mass Transfer*, vol. 40, pp. 4437–4447, 1997.

[17] N. Zuber, “Hydrodynamic aspects of boiling heat transfer,” PhD Thesis, University of California, Los Angeles, 1959.

[18] S. Sudhakar, J. A. Weibel, F. Zhou, E. M. Dede, and S. V. Garimella, “Area-scalable high-heat-flux dissipation at low thermal resistance using a capillary-fed two-layer evaporator wick,” *International Journal of Heat and Mass Transfer*, vol. 135, pp. 1346–1356, Jun. 2019.

[19] K. S. Udell, “Heat transfer in porous media considering phase change and capillarity—the heat pipe effect,” *International Journal of Heat and Mass Transfer*, vol. 28, pp. 485–495, 1985.

[20] H. H. Bau, and K. E. Torrance. "Boiling in low-permeability porous materials," *International Journal of Heat and Mass Transfer,* vol. 251, pp. 45-55, 1982.

[21] V. X. Tung and V. K. Dhir, “A hydrodynamic model for two-phase flow through porous media,” *International Journal of Multiphase Flow*, vol. 14, pp. 47–65, 1988.

[22] A. E. Scheidegger, “The physics of flow through porous media,” Third edition, *University of Toronto Press*, 1974.

[23] M. Kaviany, “Principles of heat transfer in porous media,” Second edition, Springer Science & Business Media, New York, NY, USA, 1995.

[24] S. A. Kovalev, S. L. Solov'yev, and O. A. Ovodkov, “Liquid boiling on porous surfaces,” *Heat transfer Soviet research*, vol. 19, pp.109-120, 1987.

[25] D. G. Avraam and A. C. Payatakes, “Flow regimes and relative permeabilities during steady-state two-phase flow in porous media,” *Journal of Fluid Mechanics*, vol. 293, pp. 207–236. 1995.

[26] J. M. Schembre and A. R. Kovscek, “A technique for measuring two-phase relative permeability in porous media via X-ray CT measurements,” *Journal of Petroleum Science and Engineering*, vol. 39, pp. 159–174, 2003.

[27] I. S. Hussaini and C. Y. Wang, “Measurement of relative permeability of fuel cell diffusion media,” *Journal of Power Sources*, vol. 195, pp. 3830–3840, 2010.

[28] C. Zhang, J. W. Palko, M. T. Barako, M. Asheghi, J. G. Santiago, and K. E. Goodson, “Enhanced capillary-fed boiling in copper inverse opals via template sintering,” *Advanced Functional Materials*, vol. 28, p. 1803689, 2018.

[29] J. T. Gostick, M. A. Ioannidis, M. W. Fowler, and M. D. Pritzker, "Direct measurement of the capillary pressure characteristics of water–air–gas diffusion layer systems for PEM fuel cells," *Electrochemistry Communications*, vol. 10, pp. 1520–1523, 2008.

[30] V. Joekar-Niasar, S. M. Hassanizadeh, and A. Leijnse, "Insights into the relationships among capillary pressure, saturation, interfacial area and relative permeability using pore-network modeling," *Transp Porous Med*, vol. 74, pp. 201–219, 2008.

[31] K. K. Bodla, J. Y. Murthy, and S. V. Garimella, "Direct simulation of thermal transport through sintered wick microstructures," *Journal of Heat Transfer*, vol. 134, p. 012602, 2012.

[32] A. Faghri, "Heat pipe science and technology," *Taylor & Francis*, Washington, DC, 1995.

[33] W. S. Chang, "Porosity and effective thermal conductivity of wire screens," *Journal of Heat Transfer*, vol. 112, pp. 5–9, 1990.

[34] B. S. Singh, A. Dybbs, and F. A. Lyman, "Experimental study of the effective thermal conductivity of liquid saturated sintered fiber metal wicks," *International Journal of Heat and Mass Transfer*, vol. 16, pp. 145–155, 1973.

[35] C. Li and G. P. Peterson, "The effective thermal conductivity of wire screen," *International Journal of Heat and Mass Transfer*, vol. 49, pp. 4095–4105, 2006.

[36] S. Adera, D. Antao, R. Raj and E. N. Wang, "Design of micropillar wicks for thin-film evaporation," *International Journal of Heat and Mass Transfer*, vol. 101, pp.280-294, 2016.

[37] R. Lewis, L.A. Liew, S. Xu, Y.C. Lee and R. Yang, "Microfabricated ultra-thin all-polymer thermal ground planes," *Science Bulletin*, vol. 60, pp.701-706, 2015.

[38] C. Ding, G. Soni, P. Bozorgi, B. D. Piorek, C. D. Meinhart and N. C. MacDonald, "A flat heat pipe architecture based on nanostructured titania," *Journal of Microelectromechanical Systems*, vol. 19, pp.878-884, 2010.

[39] J. A. Weibel, S. V. Garimella, and M. T. North, "Characterization of evaporation and boiling from sintered powder wicks fed by capillary action," *International Journal of Heat and Mass Transfer*, vol. 53, pp. 4204–4215. 2010.

[40] J. A. Weibel, "Characterization of fluid-thermal transport and boiling in micro/nano-engineered porous structures," Ph.D. thesis, Purdue University, Indiana, USA, 2012.

[41] C. Li, G. P. Peterson, and Y. Wang, "Evaporation/Boiling in Thin Capillary Wicks (l)—Wick Thickness Effects," *Journal of Heat Transfer*, vol. 128, pp. 1312–1319, 2006.

[42] V. P. Carey, "Liquid-vapor phase-change phenomena: An introduction to the thermophysics of vaporization and condensation processes in heat transfer equipment," Third edition, *CRC Press, Taylor and Francis Group*, 2020.